Materials Today Bio 22 (2023) 100758

Contents lists available at ScienceDirect

Materials Today Bio

journal homepage: www.journals.elsevier.com/materials-today-bio

Graphene oxide accelerates TGFβ-mediated epithelial-mesenchymal transition and stimulates pro-inflammatory immune response in amniotic epithelial cells

Adrian Cerverò-Varona [a,1], Angelo Canciello [a,*,1], Alessia Peserico [a], Arlette Alina Haidar Montes [a], Maria Rita Citeroni [a], Annunziata Mauro [a], Valentina Russo [a], Samanta Moffa [b], Serena Pilato [b], Stefano Di Giacomo [b], Beatrice Dufrusine [a], Enrico Dainese [a], Antonella Fontana [b], Barbara Barboni [a]

[a] Department of Biosciences and Agro-Food and Environmental Technologies, University of Teramo,64100, Teramo, Italy
[b] Department of Pharmacy, University "G. D'Annunzio", Via Dei Vestini, 66100, Chieti, Italy

ARTICLE INFO

Keywords:
Graphene oxide (GO)
Epithelial-mesenchymal transition (EMT)
Collective migrations
Immunomodulation
Inflammation

ABSTRACT

The application of biomaterials on immune regenerative strategies to deal with unsolved pathologies is getting attention in the field of tissue engineering. In this context, graphene oxide (GO) has been proposed as an immune-mimetic material largely used for developing stem cell-based regenerative therapies, since it has shown to influence stem cell behavior and modulate their immune response. Similarly, amniotic epithelial stem cells (AECs) are getting an increasing clinical interest as source of stem cells due to their great plasticity and immunomodulatory paracrine activities, even though GO bio-mimetic effects still remain unknown. To this aim, GO-functionalized glass coverslips have been used for AECs culture. The results demonstrated how GO-coating is able to induce and accelerate the Epithelial-Mesenchymal Transition (EMT), in a process mediated by the intracellular activation of TGFβ1-SMAD2/3 signaling pathway. The *trans*-differentiation towards mesenchymal phenotype provides AECs of migratory ability and substantially changes the pattern of cytokines secretion upon inflammatory stimulus. Indeed, GO-exposed AECs enhance their pro-inflammatory interleukins production thus inducing a more efficient activation of macrophages and, at the same time, by slightly reducing their inhibitory action on peripheral blood mononuclear cells proliferation.

Therefore, the adhesion of AECs on GO-functionalized surfaces might contribute to the generation of a tailored microenvironment useful to face both the phases of the inflammation, thereby fostering the regenerative process.

1. Introduction

Amniotic-derived stem cells isolated from placenta have been proposed as promising candidates in developing therapeutic treatments in regenerative medicine [1–4]. Amniotic epithelial cells (AECs) which are among the most studied amniotic-derived cells to date, along with the large availability, also offer many advantages such as no ethical concerns, high plasticity without any tumor derives as well as both basal and induced immunomodulatory properties [1,5].

In particular, the increasing clinical interests on AECs are mainly related to their great plasticity that had been attributed to their early embryological stage origin and to the presence of a variable subpopulation of cells expressing pluripotent markers [6–9]. The preclinical settings started to define insights the AECs pro-regenerative mechanisms expressed by combining *trans*-differentiation with paracrine activities [10]. To this regard, AECs are able to differentiate into tendon-like cells in experimental injured Achille tendons [4,11,12]. Likewise, other evidences demonstrated a similar *trans*-differentiation ability of AECs towards cardiomyocyte-like and hepatocyte-like cells [13,14].

AECs immune paracrine activity had been well documented to date in different systems to accelerate healing by promoting the transition from the inflammatory to the proliferative phase [15,16] and by

* Corresponding author.
E-mail address: acanciello@unite.it (A. Canciello).
[1] Co-first authors.

https://doi.org/10.1016/j.mtbio.2023.100758
Received 14 May 2023; Received in revised form 23 July 2023; Accepted 1 August 2023
Available online 2 August 2023

developing an anti-fibrotic action [17,18]. AECs express a basal release of immunomodulatory bioactive factors aimed physiologically to generate the immune tolerance at the barrier between the two semi-allogenic organism: mother and fetus [19,20]. However, the immunomodulatory properties of AECs are also amplified in response to inflammatory stimulus [21,22] and when the cells have been inserted in injured tissues [4]. Additionally, also tissue engineering strategies have also been proposed to potentiate the AECs immune action by seeding them on immune inductive scaffolds [23].

Alternatively, graphene oxide (GO) has been proposed as an immune mimetic material largely used for eliciting stem cell-based regenerative therapies [24,25] even though this strategy has never been tempted up to now on AECs. Indeed, GO possess exceptional properties with respect to other additives or nanomaterials. It is a one atom thick molecule and therefore its surface is widely extended with respect to its weight allowing to adsorbe/interact with a heavy amount of proteins, drugs, ligands and cell membranes. Moreover, the low cost and the ease of functionalization and therefore the possibility to tune at will properties such as water affinity, adsorption capacity towards different molecules, surface charge, to name a few, makes GO a very attractive alternative. To this regard, it has been proven that GO constructs used for cardiac regeneration were able to reduce inflammation by interacting with macrophages and decreasing the release of reactive oxygen species [26]. At the same time, evidences collected *in vitro* demonstrated that GO nanoparticles (GONPs) were able to inhibit LPS-induced interleukin 6 (IL-6) release and to stimulate IL-10 synthesis in blood cell cultures [27]. Similarly, GO enriched polypropylene suture threads buttons decreased the expression of inflammatory markers in primary human gingival fibroblasts exposed to LPS [28].

Noteworthy, GO-based treatments may regulate stem cells immune response by modulating their phenotype, in particular, by inducing the epithelial-mesenchymal transition (EMT) as demonstrated on human retinal pigment epithelial cells and lung carcinoma epithelial cells [29–31]. In presence of GO, epithelial cells demonstrated to down-regulate E-Cadherin and β-Cadherin epithelial markers while mesenchymal markers like Vimentin, N-Cadherin, α-SMA and matrix metalloproteinases (MMP-2 and MMP-9) were upregulated. Taking advantage of such a mechanism, GO was able to enhance the migration potential of epithelial stem cells, which could be crucial for accelerating wound healing [30,31]. Despite GO-based materials are revealed as great promises for biomedical applications by receiving increasing attractiveness [32–35], there is lack of information available on their effect on AECs, an emerging source of stem cell broadly proposed for the regeneration of several biological systems [36] as well as for developing stem cell based- and -free protocols for autoimmune diseases. To this aim, the present research has been designed to assess the effects of GO-loaded glass surfaces on AECs phenotype, to study the intracellular pathway involved and, finally, to verify the impact on stem-cell immune paracrine activity.

2. Materials and methods

2.1. Ethics statement

No ethic statement is required for the present research since: 1. ovine AECs and PMBS isolation have been both isolated from waste biological samples collected at the abattoir from animals slaughtered for food purposes; 2. human leukemia monocytic cell line (hTHP1) were purchased from ATCC (Manassas, Virginia, USA).

2.2. Preparation of GO suspension

An aqueous solution of 4 g/L of graphene oxide (Graphenea, Donostia San Sebastian, Spain) was added to Ultrapure MilliQ water (electric resistance >18.2 MΩ/cm), from a Millipore Corp. model Direct-Q 3 system, to reach the concentration of 20 μg/mL and bath ultrasonicated for 30 min (37 kHz, 180 W; Elmasonic P60H; Elma). The concentration of GO was checked spectrophotometrically at λ_{max} of 230 nm by using a Varian Cary 100 BIO UV–vis spectrophotometer. GO flake dimensions and ζ-potential were determined by using dynamic laser light scattering (DLS) (90plus/BI-MAS ZetaPlus multiangle particle size analyzer, Brookhaven Instrument Corp.).

2.3. Activation of substrates

The reactions were carried out by using two different supports, i.e., 16 mm and 5 mm round glass coverslips, previously washed and ultrasonicated in isopropanol and acetone. Each side of the substrates was activated with an UV-ozone lamp (PSD-UV4 Novascan UV Ozone System Base model, Novascan Technologies, Boone; NC) for 30 min to increase the hydrophilicity of the surface and to improve the covalent binding of molecules. After the activation, the substrates were incubated with a 3-(aminopropyl)triethoxysilane (APTES) (Sigma-Aldrich, ST. Louis, MO) solution 1 M in ethanol for 1 h to form the silanized derivatives and then rinsed with ethanol to remove the excess of APTES.

2.4. Preparation of GO-functionalized substrates

The GO-functionalized substrates were prepared as previously described [33]. In detail, the APTES-activated coverslips were dipped in 20 μg/mL aqueous solution of GO for 5 h. In this way, GO flakes were covalently bound to APTES amino groups, exposed on activated substrates surfaces, through epoxy ring opening reaction or amide formation with edge carboxylic groups. After the incubation, the coverslips were rinsed with Milli-Q water to get rid of any excess of GO and subsequently sterilized under UV lamp for 2 h.

2.5. AFM, FTIR and Raman spectroscopy characterization

The surface topography of GO-functionalized coverslips was investigated with AFM by using the Multimode 8 AFM microscope (Bruker, Billerica, Massachusetts) equipped with a Nanoscope V controller in Tapping in air mode. Commercial silicon cantilever RTESPA-300 (cantilever resonance frequency 300 kHz and nominal elastic constant 40 N/m) with a nominal tip radius of 8 nm was used to analyze properties such as topography across a scan size of 20 μm × 20 μm. The images were analyzed by Nanoscope Analysis 1.8 software and the bearing analysis tool was used to calculate the percentage of surface covered by GO flakes, in the form of both single layers and overlapped GO.

IR spectra were obtained using a Shimadzu IRAffinity-1S FTIR spectrophotometer (Shimadzu Italia S.r.l., Milan, Italy) equipped with a sealed and desiccated interferometer, a DLATGS (Deuterated Triglycine Sulphate Doped with L-Alanine) detector and a single reflection diamond ATR crystal (QATR 10, Shimadzu Italia S.r.l., Milan, Italy). All FTIR spectra were recorded in the range from 500 to 3500 cm^{-1} co-adding 45 interferograms at a resolution of 4 cm^{-1} with Happ–Genzel apodization. The ATR crystal was carefully cleaned before each analysis, a background was recorded for each sample and the measurements were performed in triplicate. Spectra manipulation was carried out with the software LabSolution IR version 2.27 (Shimadzu Italia S.r.l., Milan, Italy). The Raman spectra of GO-functionalized substrates were obtained by confocal and high-performance Raman microscope (XploRA PLUS, HORIBA, Japan) with deep-cooled CCD detector technology. LabSpec (Horiba, Japan) was employed to control the Raman spectroscopic system and for the optimization and processing of the acquired data. All Raman spectroscopic measurements were performed in the range of 900–1900 cm^{-1} and with a 1800-line/mm grating. A single spectrum of the sample has been detected with a 532 nm laser, with a time of 8 s and 20 accumulations. For the Raman mapping of the G band intensity, an area of 400 μm^2 was chosen by using a 100 × objective and scanned with an excitation laser of 532 nm. Raman spectra are the overlaid spectra

obtained by multivariate analysis (LabSpec 6's Multivariate Analysis module) recorded in an area of 400 μm^2, using step between the points of 400 nm through SWIFT modality with a time of 1 s of acquisition and 1 accumulation. Furthermore, a pinhole of 100 μm and a 50 μm slit were used.

2.6. AECs isolation and culture

Ovine AECs were collected from the amniotic membrane (AM) of fetuses at middle stage of gestation. AECs were collected following a previously validated protocol [37]. Freshly isolated AECs were seeded at a density of 10.000 cells/well in a 12 well/plate on commercial glass coverslip as a control (AECs) or on GO-functionalized ones (AECs + GO).

2.7. Experimental plan

The different stem cell conditions and analysis performed are summarized in Fig. 1. Briefly, freshly isolated AECs were cultured in standard condition as control (AECs on uncoated coverslip) or on GO-coated coverslip (AECs + GO) until 70–80% of confluence. Then, the culture media (CM) was replaced with serum-free medium supplemented with or without 1 μg/mL LPS for 1 h. The cultural medium was replaced again with fresh serum-free medium and the cells were cultured for further for 24 h. At the end, AECs were collected as well as the serum-free CMs by centrifuging them at 300 g for 10 min to remove cell debris. AECs were analyzed for epithelial and mesenchymal gene and protein markers, assessed for TGFβ pathway and, finally, tested for migration. CM were used for assessing cytokines and chemokines release and for performing immune biological assays on ovine PBMC and human leukemia monocytic cell line hTHP1 [38].

2.8. Gene analyses

The EMT gene markers were analyzed by Real-time qPCR and normalized to GAPDH (Table 1). The relative expression was calculated by the comparative Ct (ΔCt) [39] and expressed as fold change over freshly isolated AECs (T_0) = 1. The reaction of RT-PCR was performed in triplicate for each experimental replicate of each different biological sample (n = 3).

Table 1
Primers details used for RT-qPCR analysis (also reported in Russo V et al., 2022 [40]).

Gene	Forward	Reverse
VIM	5′-GACCAGCTCACCAACGACA-3′	5′-CTCCTCCTGCAACTTCTCCC-3′
CYTO8	5′-CTCAAAGGCCAGAGGGCTTC-3′	5′-CTTGGCCTGAGCATCCTTGA-3
SNAIL	5′-GTCGTGGGTGGAGAGCTTTG−3′	5′-TGCTGGAAAGTGAGCTCTGG−3′
TWIST	5′-GCCGGAGACCTAGATGTCATTG-3′	5′-CCACGCCCTGTTTCTTTGAAT-3′
ZEB	5′-TGGCAAAAGAAAACCCATGGAAA-3′	5′-AAAGTGACCAGGGCTCACAG-3′
GAPDH	5′-CCTGCACCACCAACTGCTTG-3′	5′-TTGAGCTCAGGGATGACCTTG-3′

2.9. Immunohistochemistry

AECs phenotype was defined by analyzing the epithelial (E-Cadherin and CYTO8) and mesenchymal (VIM) protein expression and localization by immunocytochemistry (ICC) as previously reported [21]. Nuclear counterstaining was obtained with DAPI (Vectastain) at the final dilution of 1:2000 in PBS. The omission of primary antibodies (Abs) was used as negative control. Details on Abs and dilutions are specified in Table 2. The reaction was carried out in triplicate on each biological replicate (n = 3) for each experimental condition.

2.10. ROS production and viability assay

The effects of GO on cell viability were investigated in AECs and AECs + GO by assessing ROS production and cell proliferation using, respectively, DCFDA (Cellular ROS Detection Kit:Abcam) and MTS proliferation assay (G3582, Promega). ROS detection was performed by using the fluorogenic agent 2′,7′-dichlorofluorescein diacetate (DCFDA), which is able to diffuse into the cells and be deacetylated by cellular esterases to a nonfluorescent compound, following later oxidization by ROS to 2′, 7′- dichlorofluorescein (DCF). For this purpose, both AECs and AECs + GO were plated into 96-multiwell plates at cell densities of 10,000 cells/well. Twenty-four hours later, the cells were washed with PBS and incubated with 10 μM DCFDA diluted in phenol red–free medium (DMEM F12, Corning) for 40 min at 37 °C in the dark, according to

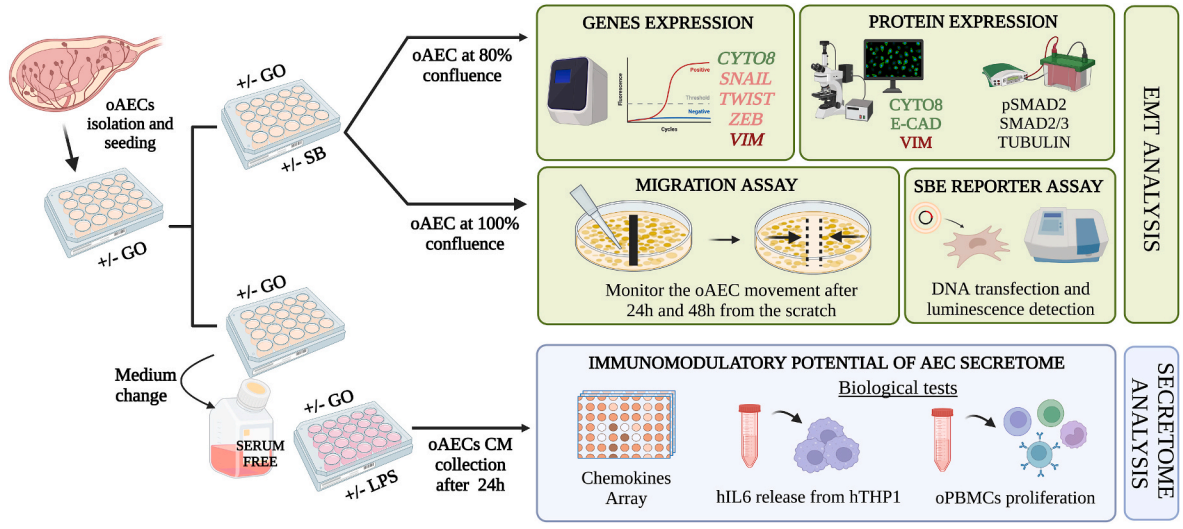

Fig. 1. Experimental design of AECs seeded on GO-coated glass coverslips. GO-induced EMT was studied by analyzing the gene expression of the CYTO8 (epithelial marker), SNAL, TWIST, ZEB (transcription factors of the EMT) and VIM (mesenchymal marker), the protein expression of CYTO8 and E-CAD (epithelial markers), VIM (mesenchymal marker) and pSMAD2, SMAD2/3 (downstream markers of TGFβ signaling pathway), the migration assay at 24 and 48 h, and the SBE reporter assay. GO-induced immunomodulatoty properties of AECs secretome was studied by analyzing the chemokine expression with a Human Inflammation Antibody Array membrane, and the biological effect on hTHP-1 and oPBMCs.

Table 2
Primary and secondary antibodies used for ICC and WB. (Ref(a) [21]; Ref(b) [40]).

Investigation	Primary Antibody	Dilution	Secondary Antibody	Dilution
ICC	E-Cadherin[a] (LS Bio, Massachusetts, USA)	1:100	Anti-rabbit Alexa Fluor (Sigma-Aldrich, St. Louis, MO, USA)	1:200
	CYTO8[a,b] (Abcam, Cambridge, UK)	1:200	Anti-mouse Alexa Fluor (Sigma-Aldrich, St. Louis, MO, USA)	1:500
	VIM[a,b] (Agilent Technologies, California, USA)	1:200	Anti-mouse Cy3 (Sigma-Aldrich, St. Louis, MO, USA)	1:750
WB	Rabbit pSMAD2[a] (3108 Cell Signalling)	1:500	Anti-rabbit HRP conjugated (31461, Pierce™ Antibody)	1:2000
	Rabbit SMAD2/3[a] (3102 Cell Signalling)	1:500	Anti-rabbit HRP conjugated (31461, Pierce™ Antibody)	1:2000
	Mouse α-TUBULIN[a] (SIGMA T5168)	1:1000	Anti-mouse HRP conjugated (Santa Cruz sc 516102)	1:10000

the provider's instructions. After an additional wash with PBS, fluorescence was evaluated at excitation of 495 nm and emission of 529 nm for 80 min by using EnSpire® Multimode Plate Reader (PerkinElmer, Waltham, MA, USA). For data analysis, blank readings were subtracted to every single measurement. On the other hand, AECs and AECs + GO cell proliferation was assessed by using CellTiter96 Aqueous One Solution Cell Proliferation Assay following manufacturer's instruction (G3582, Promega).

2.11. TGFβ pathway assessment

TGFβ and SMAD 2/3 activation was assessed by using SBE reporter. For WB analysis the total protein was extracted from each sample in lysis buffer (50 mM Tris HCl pH 8, 250 mM NaCl, 5 mM EDTA, 0.1% Triton X-100 10%) with Phosphatase Inhibitor (P5726, Sigma) and Protease Inhibitor Cocktails (P8340, Sigma) diluted according to manufacturing instruction. Samples were put on ice for 30 min, and then centrifuged at 12,000×*g* for 12 min at 4 °C. The supernatant was collected, and 5 μL of the supernatant were used to determine protein concentration with Quick Start™ Bradford 1x Dye Reagent (BioRad). Afterwards, 30 μg of total protein was separated by 10% SDS-PAGE, and then transferred to nitrocellulose membranes (BIORAD) with TURBO Transfers (BioRad). Membranes were subsequently incubated with Every blot blocking solution (Biorad) for 5 min. Primary antibodies (Table 2) were incubated overnight at 4 °C whereas specific secondary HRP conjugated IgG antibodies for 1 h, at room temperature. ClarityMax ECL reagents (LiteAblot PLUS Euroclone EMP011005) were used to detect signals with Azure Byosystem. Densitometric analysis was performed using ImageJ.

The SBE Reporter kit (Cat#: 60654, BPSBioscience) was used for monitoring the activity of TGFβ/SMAD signaling pathway in the EMT of AECs seeded on normal or GO-coated coverslips, following manufacturer's instructions. Briefly, after the cells reached 50–60% confluence, the DNA transfection was performed by using lipofectamine with the provided vectors from the kit. After 24 h of transfection, the medium was changed to serum-free medium with the activator TGFβ1 (final concentration 10 ng/mL) or the inhibitor SB-505124 (final concentration 2 μM). After 18 h of stimulation, luciferase activity was evaluated by dual-luciferase (Firefly-Renilla) reporter assay system (BPS Bioscience, 60683–1, USA) with a luminometer following manufacturer's protocol. The normalized luciferase activity of the SBE reporter was obtained by subtracting the background and the non-inducible firefly luminescence before representing the ratio of Firefly luminescence from Notch Firefly luciferase to Renilla luminescence from control Renilla luciferase.

2.12. Migration test

AECs or AECs + GO were tested for their migration properties by seeding them on 500 μm cell culture inserts (Ibidi, 80209) placed on top of normal (AEC) and GO-coated (AEC + GO) coverslips. After reaching full confluence, cells were starved for a period of 5 h in serum-free media. Then, the cell culture inserts were removed and the incubation was continued and monitored for 24 and 48 h in fresh serum-free media. The wound closure of each well was photographed using a digital camera. The percentage of wound healing and the velocity of migration was quantified by + Imagej migration plugin software [41].

2.13. Cytokine and chemokine array

Multiple pro and anti-inflammatory cytokines released in the AECs and AECs + GO, with or without LPS exposure, were detected by using a specific Human Inflammation Antibody Array (Abcam, ab134003) carried out according to the manufacturer's instructions and previously validated on ovine AEC model [42,43].

2.14. PBMCs proliferation assay

The immunomodulatory activities of AECs were analyzed on peripheral blood mononuclear cells (PBMCs) by testing their proliferation. Briefly, ovine PBMCs were obtained by density gradient centrifugation with Ficoll-Paque PLUS (Amersham Bisciences, catalogue 18-1152-69) of 16 mL peripheral blood following manufacturer's instruction. PBMCs were then activated by adding phytohemagglutinin (PHA; Sigma) at a final concentration of 2.5 μg/mL. A total of 2×10^5 of PHA stimulated PBMCs were plated and cultured for 72 h with CM derived from immune-activated AECs (LPS stimulus) seeded on normal or GO-coated coverslips. PBMCs proliferation was assessed by using CellTiter96 Aqueous One Solution Cell Proliferation Assay following manufacturer's instructions (Promega-G3582).

2.15. Analysis of hTHP1 IL6 secretion

CM biological effect on activated human macrophages was performed by assessing the IL-6 release through an ELISA assay. In detail, the human THP-1 cells were maintained in RPMI 1640 medium containing glutamine and supplemented with 10% FBS and 1 mM sodium pyruvate (Gibco; Thermo Fisher Scientific, Inc., Waltham, MA, USA). Afterwards, monocytes were differentiated into macrophages, as previously described [38]. THP-1-derived macrophages were treated with the CM diluted 1:1, with complete RPMI medium for 24 h. Thereafter, the supernatants were collected, centrifugated at 3000×*g* for 10 min at 4 °C, filtered using a 0.2 μm Ministart sterile filter (Sartorius, Varedo, Italy), and stored at −80 °C until further use. These cellular supernatants were used to quantify the concentrations of released IL-6 using the Human IL-6 Uncoated Invitrogen ELISA Kit assay (ThermoFisher, San Diego, CA, USA) according to the manufacturer's directions. The plates were read at 450 nm and the sensitivity of the ELISA assay was in the range 2–200 pg/mL.

2.16. Statistical analysis

The quantitative data were obtained by analyzing each sample in triplicate for each experimental condition performed at least in triplicate. The results were firstly assessed for distribution using Shapiro Wilks test and analyzed by *t*-test or One-way Anova test followed by Tuckey post hoc test. (GraphPad Prism 9, GraphPad Software, San Diego, CA, USA). Significant was set at $p < 0.05$.

3. Results

3.1. Characterization of GO aqueous dispersion

The concentration of the GO dispersed in Milli-Q water was checked spectrophotometrically. The UV–vis spectra showed a characteristic absorption peak at λ 230 nm (Fig. 2A), which can be attributed to the π-π* transitions for aromatic C–C bonds and a shoulder at λ 290–300 nm being the fingerprint of n- π* transitions of carbonyl groups. Preliminary DLS and ζ-potential experiments evidenced that GO dispersions comprised large-sized (average diameter of 777.1 ± 123.8 nm) and negatively charged (−25.02 ± 1.65 mV) flakes, with a polydispersity index of 0.33 ± 0.02, indicating the modest homogeneity in size of the material.

3.2. Surface characterization of GO-functionalized coverslips

AFM analysis was used to characterize the surface of the GO-functionalized supports. The analysis revealed the presence of individual GO sheets with not uniform lateral dimensions, in agreement with DLS measurements. The ultrasound vibrations of the bath sonicator, used to promote the GO dispersion, favored the breaking of the sheets into smaller and not homogeneous flakes. Isolated GO sheets were well visualized onto the surface of GO-functionalized samples. In addition, the topographical AFM analysis was employed to investigate the thickness of the GO flakes present onto coverslips surface. The AFM images were analyzed by Nanoscope Analysis 1.8 Software, tracing several topographical cross sections on the GO-functionalized area and recording the vertical distance values. The height profiles confirmed the presence of single layers of GO sheets with a thickness of few nanometers (Fig. 3A). In the same samples it was also possible to notice brighter ripples with a thickness that reached tens of nanometers, due to the random reaction of GO flakes with the APTES-activated surface and the consequent GO sheets overlapping. Moreover, the bearing analysis of AFM software performed on three different 400 μm^2 regions (Fig. 3B–D), and the relevant (Fig. 3B1-D1), revealed that GO flakes were uniformly distributed on the coverslips surface, covering the 70.4 (±5.5) % of the surface.

The chemical conjugation of GO to the coverslips was confirmed by FT-IR spectroscopy. The FTIR spectrum of GO-functionalized glass was compared to that of the glass in Fig. 2B. The presence of GO in the GO-functionalized glass was confirmed by the peak around 3300 cm^{-1} referring to the O–H stretching of GO; the peak at 1724 cm^{-1} due to the C═O stretching of carbonylic and carboxylic groups of GO and the bands between 1550 cm^{-1} and 1650 cm^{-1} highlighting the presence of the olefinic and aromatic C═C sp^2 of the hydrocarbon lattice. The band at 1250 cm^{-1} corresponding to C–N stretching confirmed the binding of GO to the silanized glass. Moreover, the two C–H stretching bands around 2900 cm^{-1} were indicative of the presence of saturated carbon in the GO structure. Eventually, the huge band of the glass around 1050 cm^{-1} due to Si–O asymmetric stretching became broader and split into two peaks, due the presence of C–O stretching in the1000-1300 cm^{-1} region.

To further confirm the distribution of GO flakes on the coverslips surface, Raman spectroscopy analysis was performed. Firstly, the single spectrum of the GO-functionalized substrate confirmed the presence of the D and G fingerprints peaks of GO centered at ~1350 and ~1600 cm^{-1} (Fig. 2C), respectively: the G band related to sp^2 hybridized carbon atoms forming the honeycomb structure, and the D peak indicative of the defects of the aromatic lattice and therefore due to edges, sp^3 carbons and bonds of carbon with oxygen atoms. Lastly, the cumulative Raman spectra obtained for a 400 μm^2 area (Fig. 2D) and the relevant Raman mapping of G band intensities on the same region (Fig. 2E) were reported. The intensity color scale of the mapping varies from dark brown, for zones without GO, to bright yellow for regions with the maximum concentration of GO. Despite the presence of dark regions, Raman spectroscopy confirmed the relatively homogeneous coverage of the analyzed surface by GO flakes, in agreement with AFM measurements.

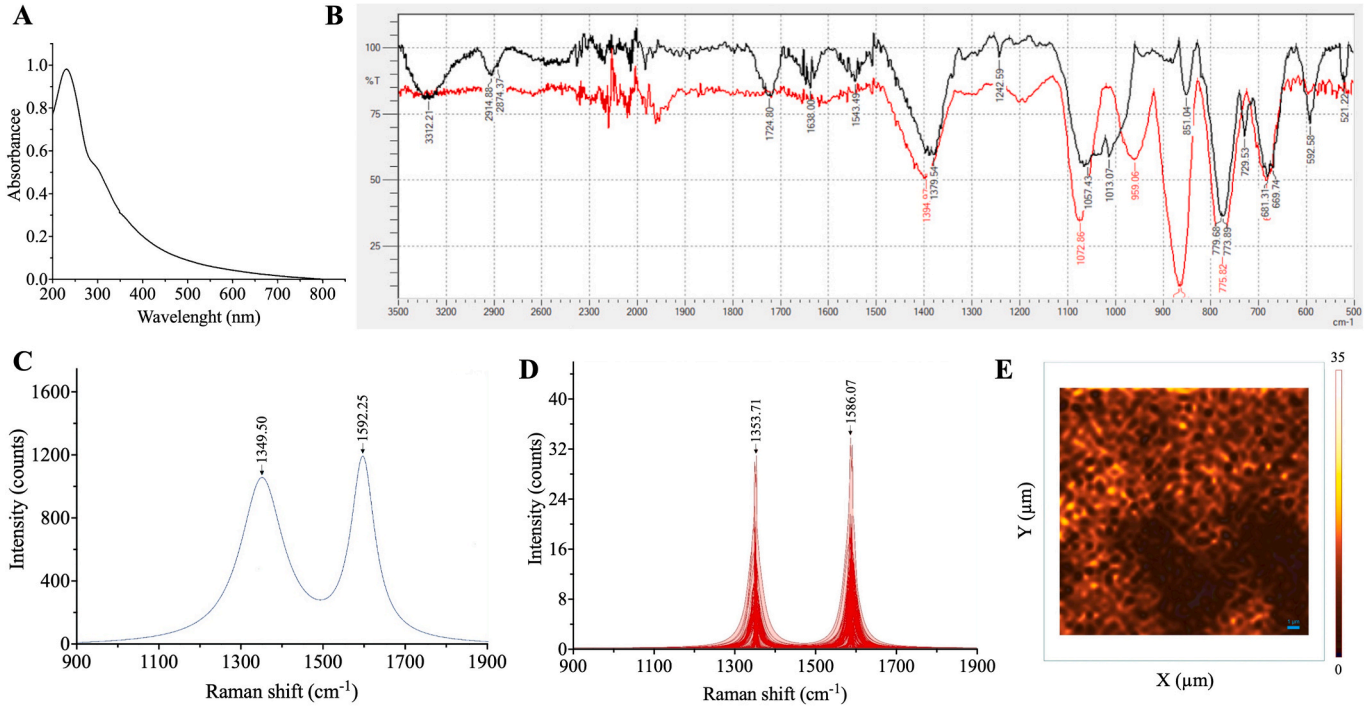

Fig. 2. (A) UV–vis spectra of 20 μg/mL GO dispersion. (B) FTIR spectra of glass coverslip (red spectrum) and GO-functionalized coverslip (black spectrum). (C) Raman spectra of GO-functionalized coverslip. (D) Cumulative Raman spectra for a 400 μm^2 area of GO-coverslip. (E) Relevant Raman mapping of D and G bands intensity on the same 400 μm^2 region. (For interpretation of the references to color in this figure legend, the reader is referred to the Web version of this article.)

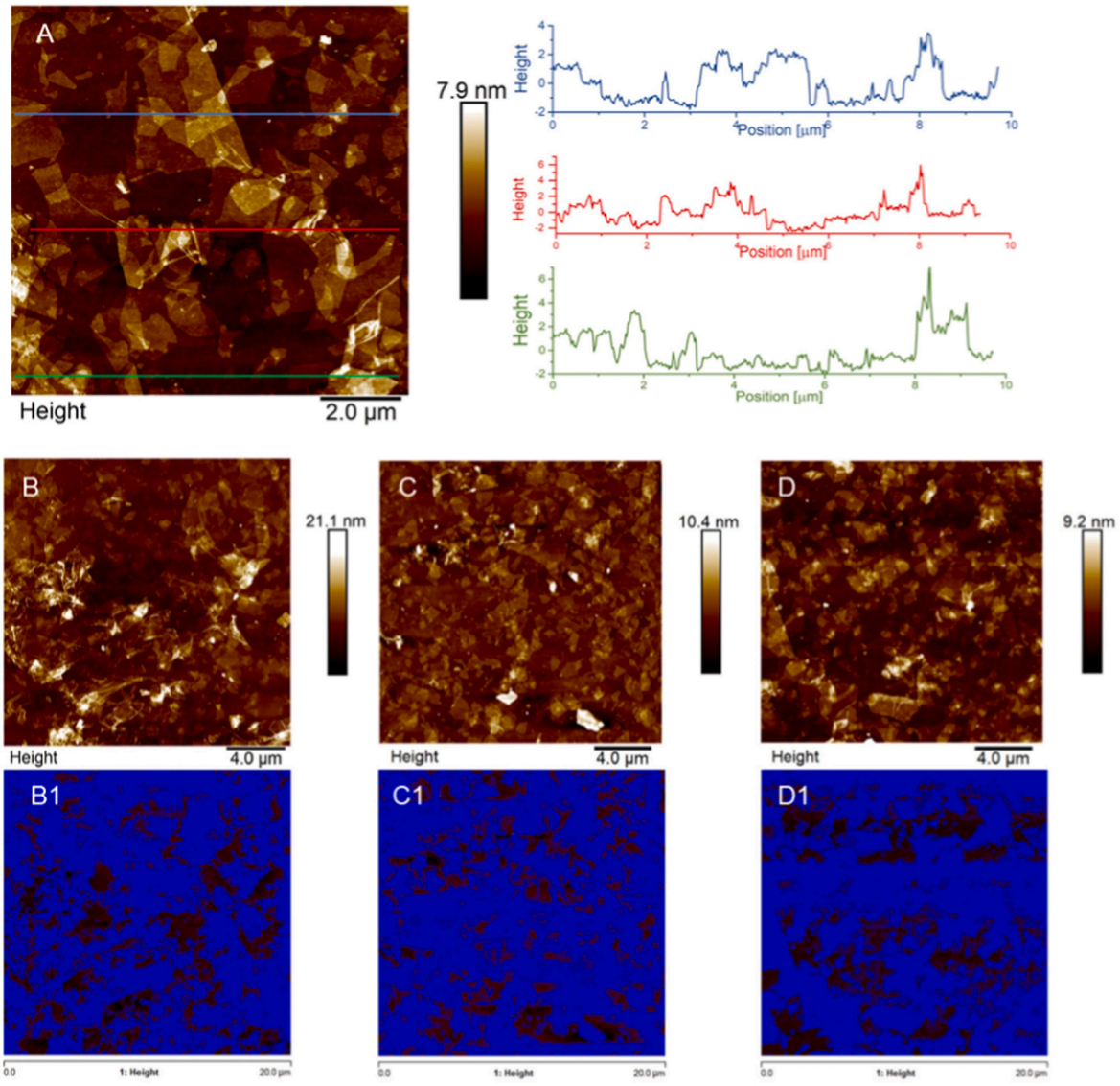

Fig. 3. (A) AFM image of surface topography and corresponding height cross-sectional profiles of GO-functionalized coverslips. (B–D) Three different AFM images of 400 µm^2 surface of GO-functionalized coverslips. (B1-D1) Images, corresponding to the surfaces depicted in B-D, in which the blue regions represent the areas covered by GO flakes, including single-layer nanosheets and overlapped GO sheets. (For interpretation of the references to color in this figure legend, the reader is referred to the Web version of this article.)

3.3. GO induces EMT in AECs

In order to assess the EMT process in AECs, the expression of epithelial and mesenchymal markers was evaluated by Real-Time PCR and immunofluorescence (Fig. 4). Gene expression data showed a downregulation of the epithelial marker CYTO8 ($p < 0.05$) and

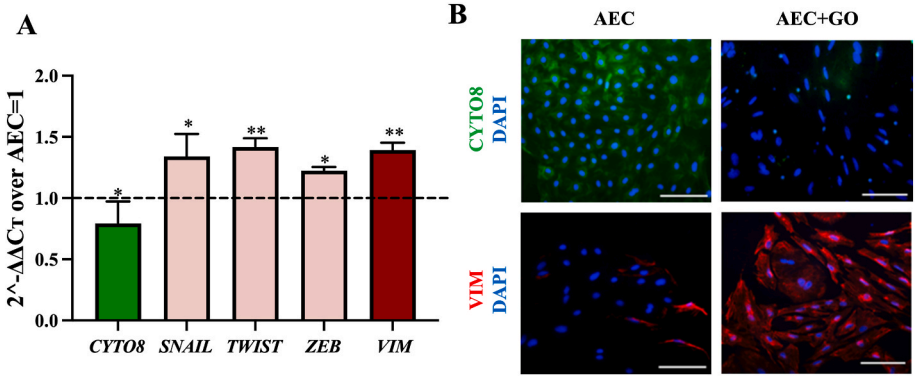

Fig. 4. (A) Genes expression analyses of EMT related markers. The graph shows the gene expression of *CYTO8, SNAIL, TWIST, ZEB* and *VIM* in the AECs + GO samples normalized on AECs = 1 (dashed line). Significance is relative to comparison with AECs obtained by *t*-test analysis and is denoted by the superscript $*p < 0.05$ and $**p < 0.01$ *vs* AECs. (B) Representative images of AECs and AECs + GO for CYTO8 (green) and VIM (red). The nuclei were colored with DAPI (blue). Magnification at 10×. Scale bar 100 µm. Values were considered significant for $p < 0.05$, with the indicated superscripts $**p < 0.01$ *vs* AECs. (For interpretation of the references to color in this figure legend, the reader is referred to the Web version of this article.)

upregulation of transcription factors SNAIL ($p < 0.05$), TWIST ($p < 0.01$), ZEB ($p < 0.05$) and late mesenchymal marker VIM ($p < 0.01$) in the samples AECs + GO compared to control AECs (Fig. 4A). Immunofluorescence results confirmed the molecular data showing greater positivity to VIM marker and a very weak presence of CYTO8 in AECs + GO samples respect to AECs that display high positivity to CYTO8 and only some cells positive to VIM (Fig. 4B). Accordingly, the cell morphology changes according to the culture conditions (data not showed).

3.4. GO induces an increase of ROS production without affecting cell viability

According to recent evidences, GO may influence cell viability due to its ability to induce an increase in ROS production [44,45]. Therefore, ROS production was measured in both AECs and AECs + GO by using DCFDA method for 80 min (Fig. 5A). Intriguingly, both AECs cultured on normal (AECs) and GO-coated coverslips (AECs + GO) showed a time-depended increase of ROS production (Fig. 5A). However, a significant difference in ROS generation was recorded from 45 to 80 min in AECs + GO compared to AECs (Fig. 5A).

In order to explore whether this increase of ROS production affected cell viability, AECs and AECs + GO were subjected to MTS-based cell proliferation assay (Fig. 5B). Notably, AECs + GO showed similar proliferation rate compared to AECs, thus suggesting that AECs viability was not affected by the GO-induced increasing of ROS production.

3.5. GO induces EMT through the activation of TGFβ1/SMAD signaling pathway

In order to study the signaling pathway involved in the GO-induced EMT on AECs it was firstly evaluated SMAD protein phosphorylation. The WB results showed an upregulation of the ratio pSMAD/SMAD on the AECs + GO in comparison to the control (Fig. 6A). Moreover, SB505124 treatment (AECs + GO + SB) was able to reduce the pSMAD/SMAD to the basal levels. On the contrary, no differences were observed on AECs and AECs + SB. To confirm the involvement of the TGFβ1/SMAD signaling pathway activation, SBE luciferase assay was used. While no luciferase activity was observed on the control, TGFβ1 stimulation (AECs + TGFβ1) markedly increased SMAD phosphorylation. (Fig. 6B). Notably, GO induced an increased luciferase activity similar to the positive control (AECs + TGFβ1), whilst the phosphorylation of SMAD induced by GO was inhibited when the cells were treated with SB505124 (AECs + GO + SB) (Fig. 6B).

3.6. GO stimulates a mesenchymal-type of collective migration

The early activation of EMT is often associated with an increase of cell migration. To this regard, the wound healing assay was performed to evaluate the effects of GO on AECs lateral migration. The results showed a similar cells clonal movement, but a faster wound closure was already evident in AECs + GO after 48 h compared to control AECs that do not show a complete closure of the wound at the same time point (Fig. 7A). This data was supported by the analyses of the percentage of closure in which was evident how AECs + GO were able to reach already the 50% of closure at 24 h compared to AECs ($p < 0.01$) (Fig. 7B).

The speed analyses showed how AECs + GO displayed an increased speed of migration at 24 h and 48 h respect to control AECs ($p < 0.005$) even though at 48 h they diminished their rate ($p < 0.01$) (Fig. 7C). On the contrary, AECs moved homogeneously and at the same speed with no significance differences recorded between 24 h and 48 h (Fig. 7C).

Finally, the double immunohistochemistry for E-Cadherin and Vimentin performed during cell migration indicated that either AECs and AECs + GO showed collective type of migration (Fig. 7D). However, AECs showed mainly membrane expression of E-Cadherin and relatively low expression of Vimentin, suggesting an epithelial type of collective migration (Fig. 7D); conversely, AECs + GO greatly increased Vimentin expression and reduced or showed cytoplasmic expression of E-Cadherin, further suggesting that these cells migrate according to a mesenchymal-type of collective migration (Fig. 7D) [46].

3.7. GO modulates AECs immune response by inducing release of either pro- and anti-inflammatory mediators

In order to determine whether GO under an inflammatory condition affects the secretion of different cytokines or chemokines, a specific Human Inflammation Antibody Array was used to test conditioned medium (CM) derived from either AECs and AECs + GO stimulated with LPS in order to recapitulate an inflammatory insult (Fig. 8). To this aim cells were treated with 1 μg/mL LPS for 1 h and then the stimulus was removed from the CM that was collected after other 24 h.

This test allowed to analyze not only anti- and pro-inflammatory cytokines but also angiogenetic factors. To this regard, it has been demonstrated how GO induced the increase of several inflammatory cytokines (such as IL3, IL16, TNF-α, TNF-β, EOTAXIN, EOTAXIN-2, MIG, IFN-γ, IL-12 p70, MIP-1δ) compared with AECs cultured under control conditions (Rantes, MIP-1β, IL-1α) when stimulated with LPS (Fig. 8). Conversely, AECs without GO up-regulated the secretion of anti-inflammatory molecules (IL-13, TGFβ1, IL-10, IL-11, I-309, IL-12 p40) respect to AECs + GO (PDGF-BB) (Fig. 8). Intriguingly, different soluble factors with angiogenetic potential were induced by the two conditions. In particular, GO increased the secretion of IL-17, sTNF RI, sTNF RII whereas AECs alone preferentially induced IL-7, M-CSF (Fig. 8).

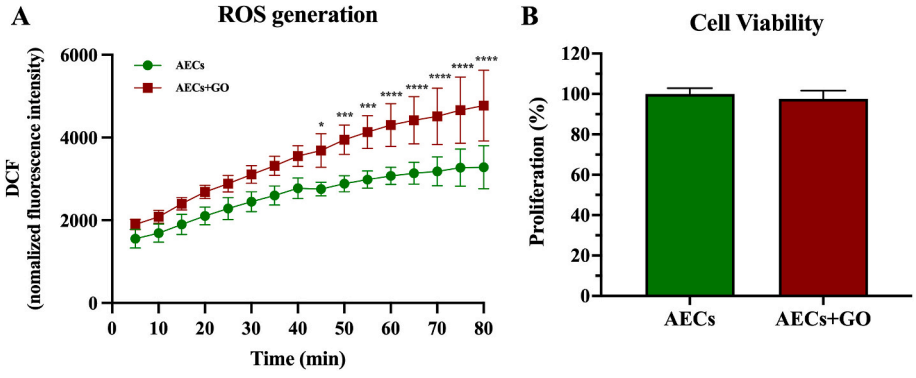

Fig. 5. AEC's viability and cytotoxicity under GO-coated coverslips exposition. (A) Reactive oxygen species (ROS) generation measured by DCFDA Cellular ROS Detection Kit on AECs seeded in normal or GO-coated coverslips. (B) Cell viability studies performed with MTS proliferation assay. Significance indicated with the superscript $*p < 0.05$, $***p < 0.001$ and $****p < 0.0001$ *vs* AECs.

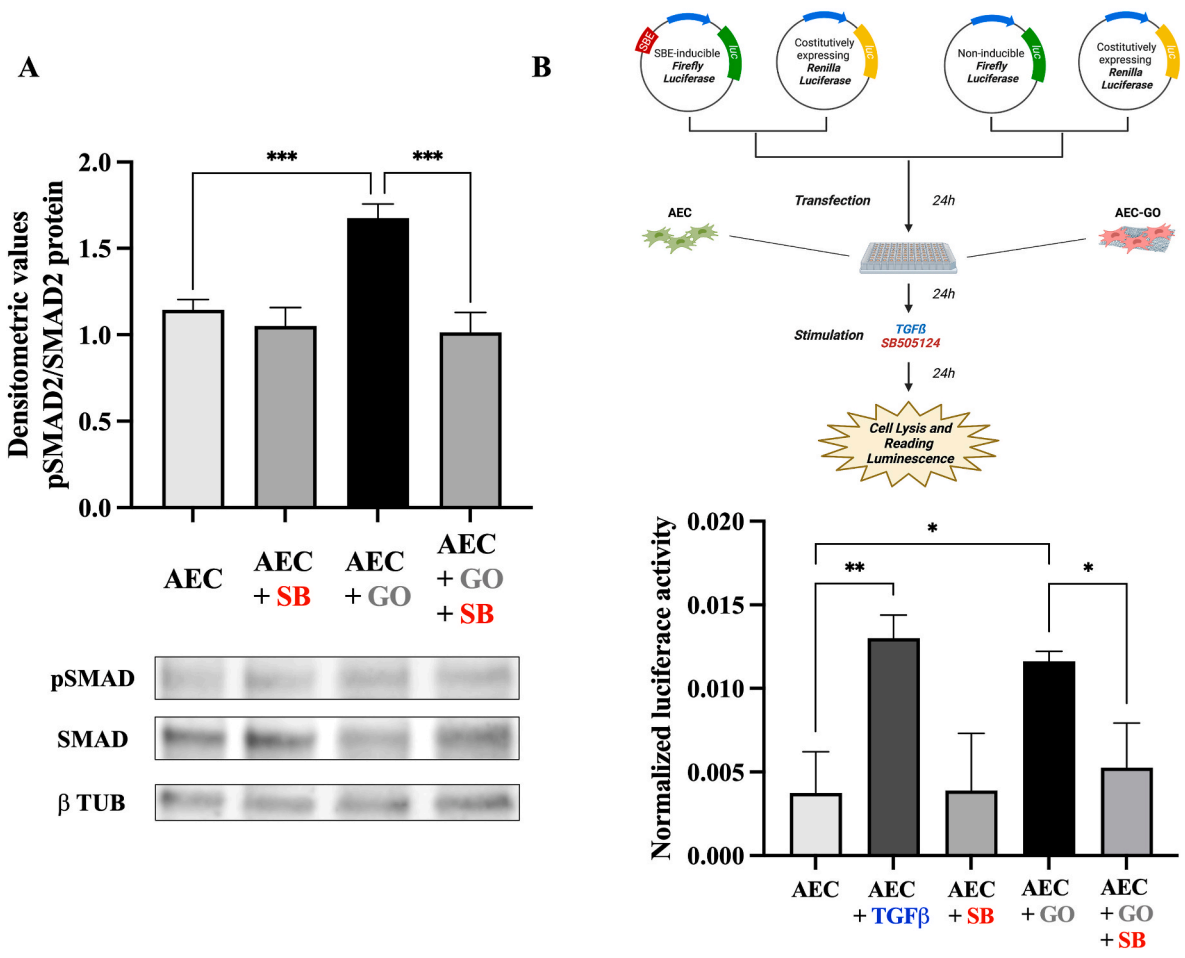

Fig. 6. TGFβ signaling pathway analysis on GO-induced EMT. (A) Western blot of SMAD2/3 and pSMAD2/3 in AECs and AECs + GO with or without SB505124. (B) Graphical representation SBE luciferase assay in order to assess TGFβ signaling pathway activation. Significance is represented with the superscript $*p < 0.05$, $**p < 0.01$ and $***p < 0.001$.

3.8. GO affects the immunomodulatory properties of AECs

In order to test the paracrine activity of CM collected from AECs and AECs + GO, proliferation of peripheral blood mononuclear cells (PBMCs) and IL-6 secretion from hTHP-1-derived macrophages has been analyzed. Proliferation of PBMCs was assessed as an index of AECs inhibitory abilities, while IL-6 secretion on THP-1-derived macrophages was assessed as an index of immune cell activation.

As result, CM derived from both AECs and AECs + GO suppressed PHA-stimulated PBMCs proliferation of 75% and 60%, respectively. Moreover, LPS stimulation further increased the reduction of PBMCs proliferation in AECs (Fig. 9). Conversely, AECs + GO stimulated with LPS showed a significant reduction in the PBMCs inhibition (Fig. 9A). In addition, CM derived from both AECs and AECs + GO stimulated with LPS induced a marked release of IL-6 with a significant increase recorded in AECs + GO (Fig. 9B).

4. Discussion

In summary, the present study demonstrated that GO coated on glass surfaces is able to accelerate EMT on ovine AECs through the TGFβ/SMAD-dependent pathway activation. In particular, this is the first instance where the immunomodulatory impact of GO has been examined emphasizing the potential of utilizing the EMT induced by this biomimetic material to target stem cell regenerative capabilities.

These results were obtained by using an *in vitro* model taking advantage of glass coverslips functionalized with micrometric GO flakes, as confirmed by FTIR analyses. Both AFM measurements and Raman spectroscopy highlighted the homogeneous and prevailingly single layer distribution of GO over the slides despite a few ripples of overlapping GO sheets were monitored by AFM. The uniform distribution of micrometric GO over the coverslips ensured that cells, seeded on the functionalized substrates, were always in contact with GO flakes thus exploiting its features. In particular, AECs could take advantages of the significant morphological and structural changes of the cellular membrane induced by GO on different cells [33] as well as its tendency to adsorb and therefore concentrate proteins on its surface [47].

Of note, no evidences of toxicity were recorded in AECs, thus indicating the safety of this support for cell culture despite that fact that GO was able to increase ROS production as similarly reported in other cell source [44,45].

However, the most impressive influence exerted by GO on AEC was the activation of signaling mechanisms inducing a massive EMT. The EMT-MET processes have been documented in AECs, a subset of epithelial stem cells, either under physiological condition during labor (by fostering the weakening of the amniotic membrane and the delivery) or under applicative biomedical procedures. More in detail, AECs may be induced towards EMT during *in vitro* expansion [37,48] or *in vivo* after transplantation into mesenchymal-derived tissues [40]. To the *in vitro* regard, AECs once isolated from amniotic membrane (AM) undergo EMT as an adaptive response to the 2D incubation within three cultural passages if not properly expanded [21,49]. Interestingly, AECs when seeded onto GO-coated coverslips show a faster EMT onset compared to CTR cells, thus suggesting the GO modulation of the mechanisms

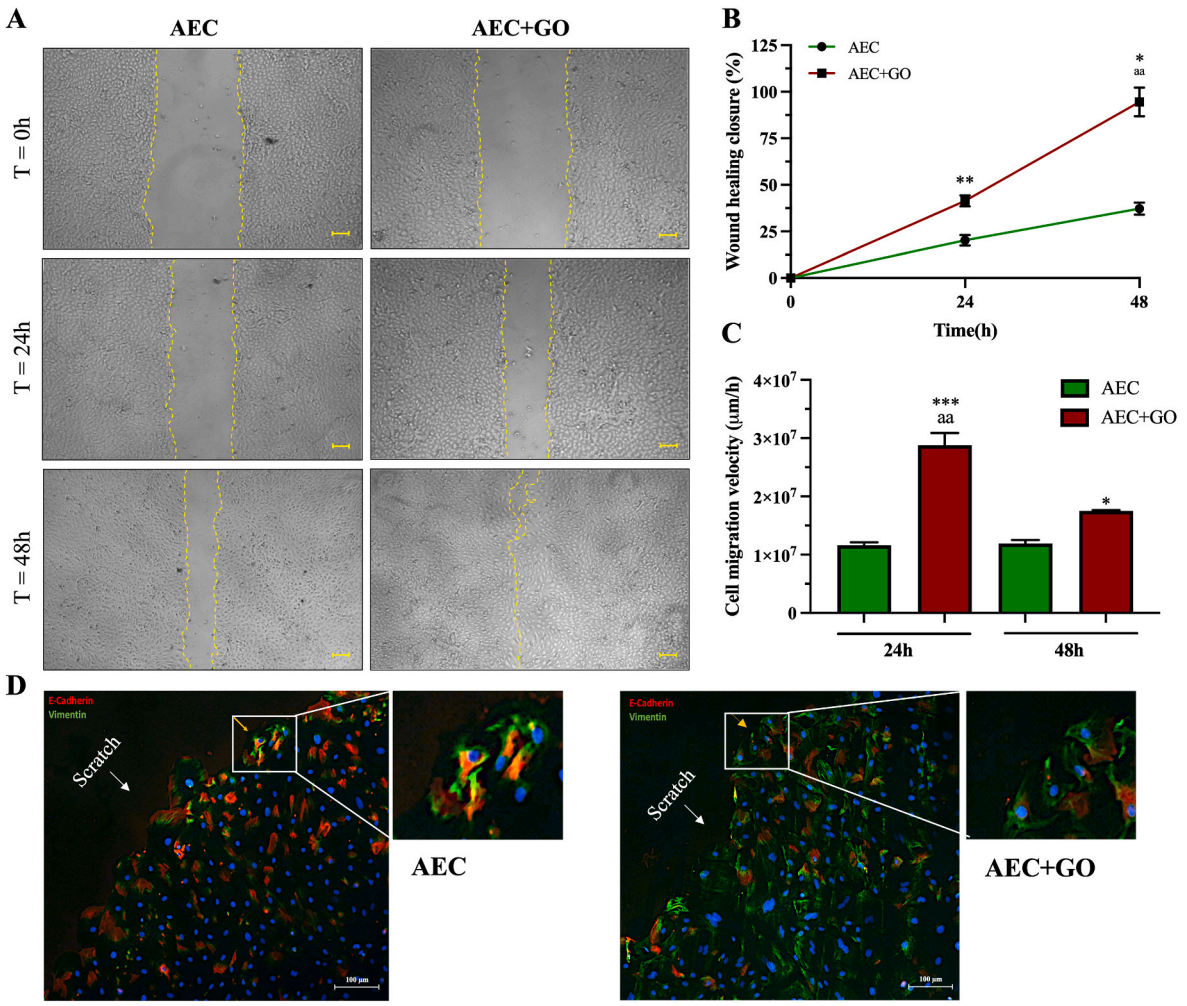

Fig. 7. Migratory potential of AECs under GO exposition. (A) Representative images of the cells migration ability under control condition (AECs) and under GO stimulation (AECs + GO) at 24 and 48 h (Scale 100 μm) (B) Representation of the percentage of wound healing closure where 0 represent the empty scratch and 100 the closed scratch. Significance is represented with the superscript $^{*}p < 0.05$ (AECs + GO *vs* AECs 48 h), $^{**}p < 0.05$ (AECs + GO *vs* AECs 24 h) and ^{aa}p<0.01 (AECs + GO 48 h *vs* AECs + GO 24 h). (C) Graphical representation of the rate of closure (μm/h). Significance is represented with the superscript $^{***}p < 0.005$ (AECs + GO *vs* AECs 24 h), $^{*}p < 0.05$ (AECs + GO *vs* AECs 48 h) and $^{aa}p<0.01$ (AECs + GO 24 h *vs* AECs + GO 48 h). (D) Immunocytochemistry of E-Cadherin (red) and Vimentin (green) on AECs (left) and AECs + GO (right) during migration. Magnification in 10×. (For interpretation of the references to color in this figure legend, the reader is referred to the Web version of this article.)

controlling cell phenotype.

The EMT-inductive action of GO has been previously demonstrated in other cell models even if the mechanisms involved remain contradictory. Liao and colleagues [29] demonstrated that reduced-GO (rGO) was able to trigger EMT activation in A549 epithelial cells within 48 h through the uptake either of nanosheets or particle aggregates of rGO via endocytosis. Consistently, Park and co-workers also reported that nano-GO (a granular material) quickly induces EMT in retinal pigment epithelium cells by activating phospholipase D (PLD) pathway [31]. Alternatively, GO-mediated EMT induction has been demonstrated to be stimulated by interactions between plasmatic membrane and GO [30] or through its passive diffusion [50]. Conversely, in the present study GO induced EMT acting at membrane level since any GO particle internalization was hooked to the coverslip thanks to covalent bounds [33].

Under similar experimental conditions, the nano-topography characteristics of the biomaterial surfaces have been proposed as drivers of *in vitro* cell behavior. Fiedler et al. demonstrated how topographically patterned interfaces with dimensions ≥10 nm influences the adhesion and proliferation of multipotent mesenchymal stromal cells and human osteoblasts [51]. Furthermore, it has been evidenced that GO-coated glass offers nanoscale topographical cues for stem cell attachment, proliferation, and differentiation [52]. In this context, several studies have observed how the surface topography of functionalized scaffolds can induce EMT by upregulating TGFβ secretion [53–56]. Indeed, TGFβ pathway is a key mechanism in promoting EMT by transcriptionally controlling a number of downstream genes [57]. The intracellular signaling is activated by TGFβR complex's receptor and operates on SMADs (SMAD2/3) effectors by inducing the serine phosphorylation upon ligand binding [58]. Similarly, the results obtained in this study seem to confirm the nano-topographical hypothesis, as GO-coated surface is able to induce EMT by activating, analogously, TGFβ-dependent mechanisms. In detail, GO induces the real time TGFβ-mediated SMAD2/3 phosphorylation promoting the shift towards mesenchymal phenotype of GO-exposed AECs.

In agreement with previous findings, GO-induced EMT enhanced AECs migration [29,31]. Of note, in this study more information on cell mobility was collected. Indeed, it has been demonstrated that GO promoted a collective cell movement thus activating a typology of migration very effective in promoting wound closure. Notably, depending on the nature of the interactions amongst cells it is possible to distinguish between two types of collective migration: (1) slow migration of tight fasten epithelial cells and (2) faster migration of mesenchymal cells

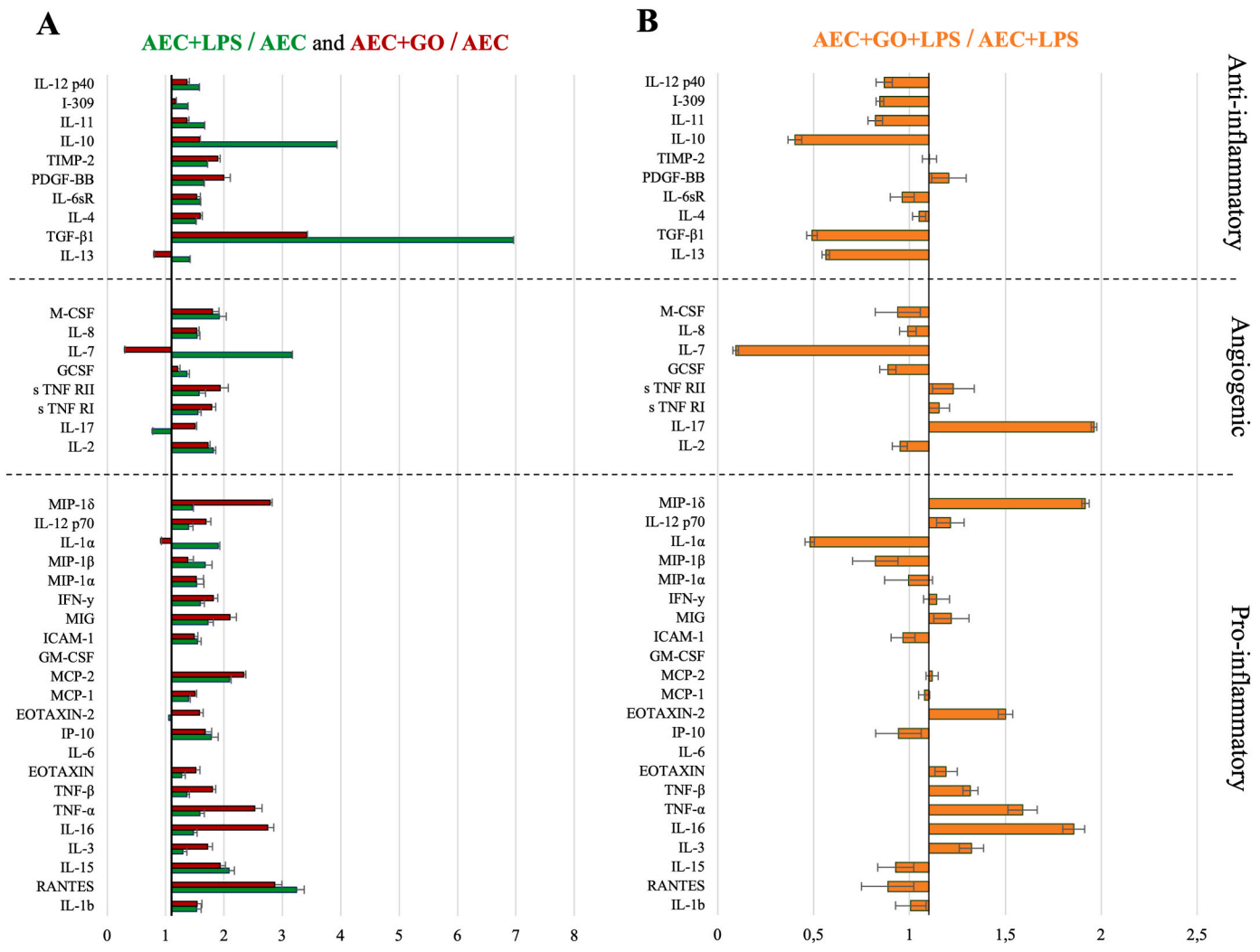

Fig. 8. Cytokines factors profile expression. (A) The layout of the array and representative images of chemokines detection. (B) Quantification by densitometric analysis of antibodies array of untreated AECs and treated samples (AECs + LPS and AECs + GO + LPS), collected after 24 h from the LPS stimulation.

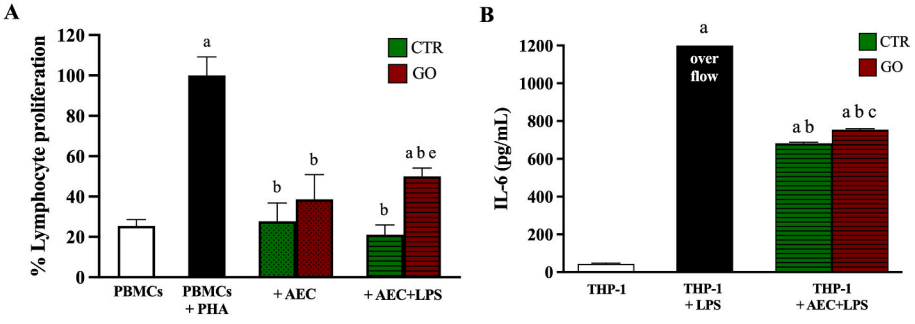

Fig. 9. Biological effect of AECs derived secretome on immune cells. (A) PBMCs proliferation assay after PHA induction and CM-AECs exposition ± GO and ± LPS. Significance is represented with the superscript; $^{a}p < 0.01$ (*vs* PBMCs); $^{b}p < 0.01$ (*vs* PBMCs + PHA); $^{c}p < 0.01$ (*vs* PBMCs + PHA + CM-AECs + LPS). (B) IL-6 secretion of hTHP-1-derived macrophages after CM-AECs + LPS exposition ± GO. Significance is represented with the superscript; $^{a}p < 0.01$ (*vs* THP-1); $^{b}p < 0.01$ (*vs* THP-1 + LPS); $^{c}p < 0.01$ (*vs* THP-1 + CM-AECs + LPS).

bearing weak heterophilic interactions [46]. In particular GO-coated surface induced in cultured AECs a mesenchymal-like collective migration highlighted by the prevalence of Vimentin positive cells on the border of the experimentally induced wound, instead of the E-cadherin positive ones recorded in control conditions, controlling an epithelial-like collective migration.

The GO-induced EMT significantly impacted also the immunomodulatory properties of AECs, both in their basal state and under inductive (LPS) conditions. The immunomodulation is exerted mainly through the paracrine/autocrine actions of the released cytokines and chemokines. Indeed, those molecules are essential in modulating the dialogue between stem cells and cells populating the damaged tissue, foremost amongst them the immune cells. Reasonably, GO-mediated immune behavior is modified in response to AECs induced mesenchymal phenotype shift, as previously reported under different experimental conditions [21,40]. For instance, GO nanosheets seem to play a role in activating M1 pro-inflammatory macrophages in a way that is strictly dependent on their size [59,60]. Furthermore, in presence of an inflammatory stimulus, GO uptake rather than inducing a strict M1-polarization, promotes the control of M1/M2 balance, thus ensuring

a facilitated innate immune response [61]. To this regard, the present results demonstrated that GO-AECs exposed to LPS enhance their pro-inflammatory interleukins production, thus inducing a more efficient activation of THP1 in releasing IL-6 and, at the same time, by reducing their inhibitory action on PBMC proliferation.

5. Conclusion

In conclusion, the adhesion of epithelial stem cells on a GO-functionalized surface might overall constitute a tailored microenvironment useful to face the inflammatory phase of the regenerative process. Indeed, GO promoting the shift of AECs towards the mesenchymal phenotype potentiates both their anti-fibrotic [62–64] and pro-regenerative actions [4,36,40,65]. In fact, AECs due to EMT enhance cell migration and the secretion of inflammatory mediators, thereby increasing the recruitment of other immune cells. Moreover, such behavior provides a favorable local condition to promote matrix remodeling [40] and endogenous progenitor activation which are both essential to speed up the wound repair by moving the inflammatory stage toward the more advanced proliferative and regenerative phases.

Credit author statement

Conceptualization, BB; Formal analysis, AC; ACV; AP; Data curation, AC; BB; Investigations, AC; ACV; AP; AHM; MC; BD; SM; SP; SDG; Resources, SM; SP; SDG; AF; Methodology, BB; AF; Supervision, BB; Validation, AC; ACV; AP; AM Visualization, AC; ACV; AP; Writing-original draft, AC; ACV; BB; AF; Writing, review & editing, BB; VR; AM; AF; ED; Founding acquisition, BB; All authors have read and agreed to the published version of the manuscript.

Declaration of competing interest

The authors declare that they have no known competing financial interests or personal relationships that could have appeared to influence the work reported in this paper.

Data availability

Data will be made available on request.

Acknowledgements

This research was funded by the European Union—Next Generation EU. Project Code: ECS00000041; Project CUP: C43C22000380007; Project Title: Innovation, digitalization, and sustainability for the diffused economy in Central Italy— VITALITY. The authors ACV and AHM were also supported by the doctorate project “Perspective for Future Innovation in Tendon Repair H2020- MSCA-ITN-EJD-P4 FIT” (Grant Agreement ID: 955685).

References

[1] C.L. Insausti, M. Blanquer, A.M. García-Hernández, G. Castellanos, J.M. Moraleda, Amniotic membrane-derived stem cells: immunomodulatory properties and potential clinical application, Stem Cells Cloning, Adv. Appl. 7 (2014) 53–63, https://doi.org/10.2147/SCCAA.S58696.

[2] Q. Liang, Z. Liu, C. Zhu, B. Wang, X. Liu, Y. Yang, X. Lv, H. Mu, K. Wang, Intrahepatic T-cell receptor β immune repertoire is essential for liver regeneration, Hepatology (2018), https://doi.org/10.1002/hep.30067.

[3] T. Miki, Amnion-derived stem cells: in quest of clinical applications, Stem Cell Res. Ther. 2 (2011) 25, https://doi.org/10.1186/scrt66.

[4] B. Barboni, V. Russo, V. Gatta, N. Bernabò, P. Berardinelli, A. Mauro, A. Martelli, L. Valbonetti, A. Muttini, O. Di Giacinto, M. Turriani, A. Silini, G. Calabrese, M. Abate, O. Parolini, L. Stuppia, M. Mattioli, Therapeutic potential of hAECs for early Achilles tendon defect repair through regeneration, J. Tissue Eng. Regen. Med. 12 (2018), e1594, https://doi.org/10.1002/term.2584. –e1608.

[5] T. Miki, Stem cell characteristics and the therapeutic potential of amniotic epithelial cells, Am. J. Reprod. Immunol. 80 (2018), e13003, https://doi.org/10.1111/aji.13003.

[6] I.L. García-Castro, G. García-López, D. Ávila-González, H. Flores-Herrera, A. Molina-Hernández, W. Portillo, E. Ramón-Gallegos, N.F. Díaz, Markers of pluripotency in human amniotic epithelial cells and their differentiation to progenitor of cortical neurons, PLoS One 10 (2015), e0146082, https://doi.org/10.1371/journal.pone.0146082.

[7] T. Miki, T. Lehmann, H. Cai, D.B. Stolz, S.C. Strom, Stem cell characteristics of amniotic epithelial cells, Stem Cell. 23 (2005) 1549–1559, https://doi.org/10.1634/stemcells.2004-0357.

[8] B. Barboni, V. Russo, V. Curini, A. Martelli, P. Berardinelli, A. Mauro, M. Mattioli, M. Marchisio, P. Bonassi Signoroni, O. Parolini, A. Colosimo, Gestational stage affects amniotic epithelial cells phenotype, methylation status, immunomodulatory and stemness properties, Stem Cell Rev. Reports 10 (2014) 725–741, https://doi.org/10.1007/s12015-014-9519-y.

[9] E. Resca, M. Zavatti, T. Maraldi, L. Bertoni, F. Beretti, M. Guida, G.B. La Sala, P. V. Guillot, A.L. David, N.J. Sebire, A. De Pol, P. De Coppi, Enrichment in c-Kit improved differentiation potential of amniotic membrane progenitor/stem cells, Placenta 36 (2015) 18–26, https://doi.org/10.1016/j.placenta.2014.11.002.

[10] B. Barboni, V. Russo, P. Berardinelli, A. Mauro, L. Valbonetti, H. Sanyal, A. Canciello, L. Greco, A. Muttini, V. Gatta, L. Stuppia, M. Mattioli, Placental stem cells from domestic animals: translational potential and clinical relevance, Cell Transplant. (2018), https://doi.org/10.1177/0963689717724797.

[11] B. Barboni, V. Curini, V. Russo, A. Mauro, O. Di Giacinto, M. Marchisio, M. Alfonsi, M. Mattioli, Indirect Co-culture with tendons or tenocytes can program amniotic epithelial cells towards stepwise tenogenic differentiation, PLoS One 7 (2012), e30974, https://doi.org/10.1371/journal.pone.0030974.

[12] B. Barboni, V. Russo, V. Curini, A. Mauro, A. Martelli, A. Muttini, N. Bernabò, L. Valbonetti, M. Marchisio, O. Di Giacinto, P. Berardinelli, M. Mattioli, Achilles tendon regeneration can be improved by amniotic epithelial cell allotransplantation, Cell Transplant. 21 (2012) 2377–2395, https://doi.org/10.3727/096368912X638892.

[13] F. Marongiu, R. Gramignoli, K. Dorko, T. Miki, A.R. Ranade, M. Paola Serra, S. Doratiotto, M. Sini, S. Sharma, K. Mitamura, T.L. Sellaro, V. Tahan, K.J. Skvorak, E.C.S. Ellis, S.F. Badylak, J.C. Davila, R. Hines, E. Laconi, S.C. Strom, Hepatic differentiation of amniotic epithelial cells, Hepatology 53 (2011) 1719–1729, https://doi.org/10.1002/hep.24255.

[14] C.-H. Fang, J. Jin, J.-H. Joe, Y.-S. Song, B.-I. So, S.M. Lim, G.J. Cheon, S.-K. Woo, J.-C. Ra, Y.-Y. Lee, K.-S. Kim, In vivo differentiation of human amniotic epithelial cells into cardiomyocyte-like cells and cell transplantation effect on myocardial infarction in rats: comparison with cord blood and adipose tissue-derived mesenchymal stem cells, Cell Transplant. 21 (2012) 1687–1696, https://doi.org/10.3727/096368912X653039.

[15] A. Mauro, V. Russo, L. Di Marcantonio, P. Berardinelli, A. Martelli, A. Muttini, M. Mattioli, B. Barboni, M1 and M2 macrophage recruitment during tendon regeneration induced by amniotic epithelial cell allotransplantation in ovine, Res. Vet. Sci. 105 (2016) 92–102, https://doi.org/10.1016/j.rvsc.2016.01.014.

[16] G. Pietrosi, A. Fernández-Iglesias, M. Pampalone, M. Ortega-Ribera, J.J. Lozano, H. García-Calderó, L. Abad-Jordà, P.G. Conaldi, O. Parolini, G. Vizzini, A. Luca, J. Bosch, J. Gracia-Sancho, Human amniotic stem cells improve hepatic microvascular dysfunction and portal hypertension in cirrhotic rats, Liver Int. 40 (2020) 2500–2514, https://doi.org/10.1111/liv.14610.

[17] H. Li, J.Y. Niederkorn, S. Neelam, E. Mayhew, R.A. Word, J.P. McCulley, H. Alizadeh, Immunosuppressive factors secreted by human amniotic epithelial cells, Investig. Ophthalmol. Vis. Sci. 46 (2005) 900–907, https://doi.org/10.1167/iovs.04-0495.

[18] T.Ž. Ramuta, M.E. Kreft, Human amniotic membrane and amniotic membrane–derived cells: how far are we from their use in regenerative and reconstructive urology? Cell Transplant. (2018) https://doi.org/10.1177/0963689717725528.

[19] A.B. Hamilton, A.G. Betz, Gimme Shelter - the Immune System during Pregnancy (Munoz-Suano 2011) (Impressão Ok), vol. 241, pdf, 2011, pp. 20–38.

[20] J.M. Ilarregui, D.O. Croci, G. a Bianco, M. a Toscano, M. Salatino, M.E. Vermeulen, J.R. Geffner, G. a Rabinovich, Tolerogenic signals delivered by dendritic cells to T cells through a galectin-1-driven immunoregulatory circuit involving interleukin 27 and interleukin 10, Nat. Immunol. 10 (2009) 981–991, https://doi.org/10.1038/ni.1772.

[21] A. Canciello, V. Russo, P. Berardinelli, N. Bernabò, A. Muttini, M. Mattioli, B. Barboni, Progesterone prevents epithelial-mesenchymal transition of ovine amniotic epithelial cells and enhances their immunomodulatory properties, Sci. Rep. 7 (2017) 3761, https://doi.org/10.1038/s41598-017-03908-1.

[22] A. Canciello, G. Teti, E. Mazzotti, M. Falconi, V. Russo, A. Giordano, B. Barboni, Progesterone prolongs viability and anti-inflammatory functions of explanted preterm ovine amniotic membrane, Front. Bioeng. Biotechnol. (2020), https://doi.org/10.3389/fbioe.2020.00135.

[23] V. Russo, M. El Khatib, G. Prencipe, A. Cerveró-Varona, M.R. Citeroni, A. Mauro, P. Berardinelli, M. Faydaver, A.A. Haidar-Montes, M. Turriani, O. Di Giacinto, M. Raspa, F. Scavizzi, F. Bonaventura, L. Liverani, A.R. Boccaccini, B. Barboni, Scaffold-mediated immunoengineering as innovative strategy for tendon regeneration, Cells 11 (2022) 266, https://doi.org/10.3390/cells11020266.

[24] M. Maleki, R. Zarezadeh, M. Nouri, A.R. Sadigh, F. Pouremamali, Z. Asemi, H. S. Kafil, F. Alemi, B. Yousefi, Graphene oxide: a promising material for regenerative medicine and tissue engineering, Biomol. Concepts 11 (2020) 182–200, https://doi.org/10.1515/bmc-2020-0017.

[25] J. Saleem, L. Wang, C. Chen, Immunological effects of graphene family nanomaterials, NanoImpact 5 (2017) 109–118, https://doi.org/10.1016/j.impact.2017.01.005.

[26] J. Han, Y.S. Kim, M.-Y. Lim, H.Y. Kim, S. Kong, M. Kang, Y.W. Choo, J.H. Jun, S. Ryu, H. Jeong, J. Park, G.-J. Jeong, J.-C. Lee, G.H. Eom, Y. Ahn, B.-S. Kim, Dual roles of graphene oxide to attenuate inflammation and elicit timely polarization of macrophage phenotypes for cardiac repair, ACS Nano 12 (2018) 1959, https://doi.org/10.1021/acsnano.7b09107. –1977.

[27] K. Lategan, H. Alghadi, M. Bayati, M. de Cortalezzi, E. Pool, Effects of graphene oxide nanoparticles on the immune system biomarkers produced by RAW 264.7 and human whole blood cell cultures, Nanomaterials 8 (2018) 125, https://doi.org/10.3390/nano8020125.

[28] L. Fonticoli, F. Diomede, A. Nanci, A. Fontana, Y. Della Rocca, D. Guadarrama Bello, S. Pilato, O. Trubiani, J. Pizzicannella, G.D. Marconi, Enriched graphene oxide-polypropylene suture threads buttons modulate the inflammatory pathway induced by Escherichia coli lipopolysaccharide, Int. J. Mol. Sci. 24 (2023) 6622, https://doi.org/10.3390/ijms24076622.

[29] Y. Liao, W. Wang, X. Huang, Y. Sun, S. Tian, P. Cai, Reduced graphene oxide triggered epithelial-mesenchymal transition in A549 cells, Sci. Rep. 8 (2018), 15188, https://doi.org/10.1038/s41598-018-33414-x.

[30] J. Zhu, B. Li, M. Xu, R. Liu, T. Xia, Z. Zhang, Y. Xu, S. Liu, Graphene oxide promotes cancer metastasis through associating with plasma membrane to promote TGF-β signaling-dependent epithelial–mesenchymal transition, ACS Nano 14 (2020) 818–827, https://doi.org/10.1021/acsnano.9b07891.

[31] S.Y. Park, W.C. Song, B. Kim, J.-W. Oh, G. Park, Nano-graphene oxide-promoted epithelial–mesenchymal transition of human retinal pigment epithelial cells through regulation of phospholipase D signaling, Nanomaterials 11 (2021) 2546, https://doi.org/10.3390/nano11102546.

[32] R. Di Carlo, A. Di Crescenzo, S. Pilato, A. Ventrella, A. Piattelli, L. Recinella, A. Chiavaroli, S. Giordani, M. Baldrighi, A. Camisasca, B. Zavan, M. Falconi, A. Cataldi, A. Fontana, S. Zara, Osteoblastic differentiation on graphene oxide-functionalized titanium surfaces: an in vitro study, Nanomaterials 10 (2020) 654, https://doi.org/10.3390/nano10040654.

[33] S. Pilato, S. Moffa, G. Siani, F. Diomede, O. Trubiani, J. Pizzicannella, D. Capista, M. Passacantando, P. Samorì, A. Fontana, 3D graphene oxide-polyethylenimine scaffolds for cardiac tissue engineering, ACS Appl. Mater. Interfaces (2023), https://doi.org/10.1021/acsami.3c00216.

[34] M. Di Giulio, R. Zappacosta, S. Di Lodovico, E. Di Campli, G. Siani, A. Fontana, L. Cellini, Antimicrobial and antibiofilm efficacy of graphene oxide against chronic wound microorganisms, Antimicrob. Agents Chemother. 62 (2018), https://doi.org/10.1128/AAC.00547-18.

[35] M. Radunovic, M. De Colli, P. De Marco, C. Di Nisio, A. Fontana, A. Piattelli, A. Cataldi, S. Zara, Graphene oxide enrichment of collagen membranes improves DPSCs differentiation and controls inflammation occurrence, J. Biomed. Mater. Res., Part A 105 (2017) 2312–2320, https://doi.org/10.1002/jbm.a.36085.

[36] A.R. Silini, O. Parolini, Placental cells and derivatives, Cell Transplant. 27 (2018) 1–2, https://doi.org/10.1177/0963689717745332.

[37] A. Canciello, L. Greco, V. Russo, B. Barboni, Amniotic epithelial cell culture, Methods Mol. Biol. (2018), https://doi.org/10.1007/978-1-4939-8600-2_7.

[38] B. Dufrusine, A. Di Francesco, S. Oddi, L. Scipioni, C.B. Angelucci, C. D'Addario, M. Serafini, A.-K. Häfner, D. Steinhilber, M. Maccarrone, E. Dainese, Iron-dependent trafficking of 5-lipoxygenase and impact on human macrophage activation, Front. Immunol. 10 (2019), https://doi.org/10.3389/fimmu.2019.01347.

[39] K.J. Livak, T.D. Schmittgen, Analysis of relative gene expression data using real-time quantitative PCR and the 2−ΔΔCT method, Methods 25 (2001) 402–408, https://doi.org/10.1006/meth.2001.1262.

[40] V. Russo, A. Mauro, A. Peserico, O. Di Giacinto, M. El Khatib, M.R. Citeroni, E. Rossi, A. Canciello, E. Mazzotti, B. Barboni, Tendon healing response is dependent on epithelial–mesenchymal–tendon transition state of amniotic epithelial stem cells, Biomedicines 10 (2022) 1177, https://doi.org/10.3390/biomedicines10051177.

[41] I. del Molino del Barrio, G. Wilkins, A. Meeson, S. Ali, J. Kirby, Breast Cancer, An examination of the potential of ACKR3 to modify the response of CXCR4 to CXCL12, Int. J. Mol. Sci. 19 (2018) 3592, https://doi.org/10.3390/ijms19113592.

[42] V. Russo, M. El Khatib, G. Prencipe, A. Mauro, O. Di Giacinto, A.A. Haidar-Montes, F. Pulcini, B. Dufrusine, A. Cerveró-Varona, M. Faydaver, C. Di Berardino, E. Dainese, P. Berardinelli, M. Schnabelrauch, B. Barboni, Tendon 3D scaffolds establish a tailored microenvironment instructing paracrine mediated regenerative amniotic epithelial stem cells potential, Biomedicines 10 (2022) 2578, https://doi.org/10.3390/biomedicines10102578.

[43] M. Di Mattia, A. Mauro, S. Delle Monache, F. Pulcini, V. Russo, P. Berardinelli, M. R. Citeroni, M. Turriani, A. Peserico, B. Barboni, Hypoxia-mimetic CoCl2 agent enhances pro-angiogenic activities in ovine amniotic epithelial cells-derived conditioned medium, Cells 11 (2022) 461, https://doi.org/10.3390/cells11030461.

[44] M. Pelin, L. Fusco, C. Martín, S. Sosa, J. Frontiñán-Rubio, J.M. González-Domínguez, M. Durán-Prado, E. Vázquez, M. Prato, A. Tubaro, Graphene and graphene oxide induce ROS production in human HaCaT skin keratinocytes: the role of xanthine oxidase and NADH dehydrogenase, Nanoscale 10 (2018) 11820–11830, https://doi.org/10.1039/C8NR02933D.

[45] J. Shen, J. Dong, F. Shao, J. Zhao, L. Gong, H. Wang, W. Chen, Y. Zhang, Y. Cai, Graphene oxide induces autophagy and apoptosis via the ROS-dependent AMPK/mTOR/ULK-1 pathway in colorectal cancer cells, Nanomedicine 17 (2022) 591–605, https://doi.org/10.2217/nnm-2022-0030.

[46] A. Canciello, A. Cerveró-Varona, A. Peserico, A. Mauro, V. Russo, A. Morrione, A. Giordano, B. Barboni, "In medio stat virtus": insights into hybrid E/M phenotype attitudes, Front. Cell Dev. Biol. 10 (2022), https://doi.org/10.3389/fcell.2022.1038841.

[47] H. Li, K. Fierens, Z. Zhang, N. Vanparijs, M.J. Schuijs, K. Van Steendam, N. Feiner Gracia, R. De Rycke, T. De Beer, A. De Beuckelaer, S. De Koker, D. Deforce, L. Albertazzi, J. Grooten, B.N. Lambrecht, B.G. De Geest, Spontaneous protein adsorption on graphene oxide nanosheets allowing efficient intracellular vaccine protein delivery, ACS Appl. Mater. Interfaces 8 (2016) 1147–1155, https://doi.org/10.1021/acsami.5b08963.

[48] L.S. Richardson, R.N. Taylor, R. Menon, Reversible EMT and MET mediate amnion remodeling during pregnancy and labor, Sci. Signal. 13 (2020) 139–148, https://doi.org/10.1126/scisignal.aay1486.

[49] A. Alcaraz, A. Mrowiec, C.L. Insausti, E.M. García-Vizcaíno, C. Ruiz-Canada, M. C. López-Martínez, J.M. Moraleda, F.J. Nicolás, Autocrine TGF-β induces epithelial to mesenchymal transition in human amniotic epithelial cells, Cell Transplant. 22 (2013) 1351–1367, https://doi.org/10.3727/096368912X657387.

[50] T. Lammel, P. Boisseaux, M.-L. Fernández-Cruz, J.M. Navas, Internalization and cytotoxicity of graphene oxide and carboxyl graphene nanoplatelets in the human hepatocellular carcinoma cell line Hep G2, Part, Fibre Toxicol 10 (2013) 27, https://doi.org/10.1186/1743-8977-10-27.

[51] J. Fiedler, B. Özdemir, J. Bartholomä, A. Plettl, R.E. Brenner, P. Ziemann, The effect of substrate surface nanotopography on the behavior of multipotnent mesenchymal stromal cells and osteoblasts, Biomaterials 34 (2013) 8851–8859, https://doi.org/10.1016/j.biomaterials.2013.08.010.

[52] A. Savchenko, R.T. Yin, D. Kireev, I.R. Efimov, E. Molokanova, Graphene-based scaffolds: fundamentals and applications for cardiovascular tissue engineering, Front. Bioeng. Biotechnol. 9 (2021), https://doi.org/10.3389/fbioe.2021.797340.

[53] C. Zhang, H. Yuan, H. Liu, X. Chen, P. Lu, T. Zhu, L. Yang, Z. Yin, B.C. Heng, Y. Zhang, H. Ouyang, Well-aligned chitosan-based ultrafine fibers committed teno-lineage differentiation of human induced pluripotent stem cells for Achilles tendon regeneration, Biomaterials 53 (2015) 716–730, https://doi.org/10.1016/j.biomaterials.2015.02.051.

[54] X. Xu, L. Ma, Y. Wu, L. Tang, Micropillar-based culture platform induces epithelial-mesenchymal transition in the alveolar epithelial cell line, J. Biomed. Mater. Res., Part A 106 (2018) 3165–3174, https://doi.org/10.1002/jbm.a.36511.

[55] Y.K. Girard, C. Wang, S. Ravi, M.C. Howell, J. Mallela, M. Alibrahim, R. Green, G. Hellermann, S.S. Mohapatra, S. Mohapatra, A 3D fibrous scaffold inducing tumoroids: a platform for anticancer drug development, PLoS One 8 (2013), e75345, https://doi.org/10.1371/journal.pone.0075345.

[56] F.F.R. Damanik, T.C. Rothuizen, C. van Blitterswijk, J.I. Rotmans, L. Moroni, Towards an in vitro model mimicking the foreign body response: tailoring the surface properties of biomaterials to modulate extracellular matrix, Sci. Rep. 4 (2014) 6325, https://doi.org/10.1038/srep06325.

[57] Y. Tsubakihara, A. Moustakas, Epithelial-mesenchymal transition and metastasis under the control of transforming growth factor β, Int. J. Mol. Sci. 19 (2018) 3672, https://doi.org/10.3390/ijms19113672.

[58] F. Xie, L. Ling, H. Van Dam, F. Zhou, L. Zhang, TGF-& beta; signaling in cancer metastasis, Acta Biochim. Biophys. Sin. 50 (2018) 121–132, https://doi.org/10.1093/abbs/gmx123.

[59] J. Ma, R. Liu, X. Wang, Q. Liu, Y. Chen, R.P. Valle, Y.Y. Zuo, T. Xia, S. Liu, Crucial role of lateral size for graphene oxide in activating macrophages and stimulating pro-inflammatory responses in cells and animals, ACS Nano 9 (2015) 10498–10515, https://doi.org/10.1021/acsnano.5b04751.

[60] R. Diez-Orejas, M.J. Feito, M. Cicuéndez, L. Casarrubios, J.M. Rojo, M.T. Portolés, Graphene oxide nanosheets increase Candida albicans killing by pro-inflammatory and reparative peritoneal macrophages, Colloids Surf. B Biointerfaces 171 (2018) 250–259, https://doi.org/10.1016/j.colsurfb.2018.07.027.

[61] M.J. Feito, R. Diez-Orejas, M. Cicuéndez, L. Casarrubios, J.M. Rojo, M.T. Portolés, Characterization of M1 and M2 polarization phenotypes in peritoneal macrophages after treatment with graphene oxide nanosheets, Colloids Surf. B Biointerfaces 176 (2019) 96–105, https://doi.org/10.1016/j.colsurfb.2018.12.063.

[62] A. Silini, O. Parolini, B. Huppertz, I. Lang, Soluble factors of amnion-derived cells in treatment of inflammatory and fibrotic pathologies, Curr. Stem Cell Res. Ther. 8 (2013) 6–14, https://doi.org/10.2174/1574888X11308010003.

[63] N. Andrewartha, G. Yeoh, Human amnion epithelial cell therapy for chronic liver disease, Stem Cell. Int. (2019) (2019) 1–10, https://doi.org/10.1155/2019/8106482.

[64] H. Wang, Y. Tian, X. Li, M. Yang, Y. Yan, Amniotic mesenchymal stem cells derived hepatocyte-like cells attenuated liver fibrosis more efficiently by mixed-cell transplantation, Int. J. Physiol. Pathophysiol. Pharmacol. 12 (2020) 11–24. http://www.ncbi.nlm.nih.gov/pubmed/32211118.

[65] A.R. Silini, A. Cargnoni, M. Magatti, S. Pianta, O. Parolini, The long path of human placenta, and its derivatives, in regenerative medicine, Front. Bioeng. Biotechnol. 3 (2015), https://doi.org/10.3389/fbioe.2015.00162.